J. Fluid Mech. (2007), *vol.* 571, *pp.* 439–454.
doi:10.1017/S0022112006003387 Printed in the United Kingdom

Drag and lift forces on bubbles in a rotating flow

By ERNST A. VAN NIEROP[1,2], STEFAN LUTHER[1], JOHANNA J. BLUEMINK[1], JACQUES MAGNAUDET[3], ANDREA PROSPERETTI[1,4] AND DETLEF LOHSE[1]

[1]Faculty of Applied Sciences, Physics of Fluids, University of Twente, The Netherlands
[2]Division of Engineering and Applied Sciences, Harvard University, Cambridge, MA 02138, USA
[3]Institut de Mécanique des Fluides de Toulouse, (IMFT), Allée du Professeur Camille Soula, 31400 Toulouse, France
[4]Department of Mechanical Engineering, Johns Hopkins University, Baltimore, MD 21218, USA

(Received 18 January 2006 and in revised form 20 July 2006)

The motion of small air bubbles in a horizontal solid-body rotating flow is investigated experimentally. Bubbles with a typical radius of 1 mm are released in a liquid-filled horizontally rotating cylinder. We measure the transient motion of the bubbles in solid-body rotation and their final equilibrium position from which we compute drag and lift coefficients for a wide range of dimensionless shear rates $0.1 < Sr < 2$ (Sr is the velocity difference over one bubble diameter divided by the slip velocity of the bubble) and Reynolds numbers $0.01 < Re < 500$ (Re is based on the slip velocity and bubble diameter). For large Sr, we find that the drag force is increased by the shear rate. The lift force shows strong dependence on viscous effects. In particular, for $Re < 5$, we measure negative lift forces, in line with theoretical predictions.

1. Introduction

Bubbly flows are of great importance in many technical and environmental questions and applications. Therefore, understanding the dynamics of bubbles and the forces acting on them is a central issue in work on multi-phase flow. These forces result from the integrated stresses acting on their (deformable) surfaces. A full numerical treatment is possible only for a limited number of bubbles. For instance, Tryggvason *et al.* (2001) could simulate, at most, a few hundred bubbles, rising at moderate Reynolds number ($Re = 20$–30), by employing a front-tracking method. To be able to track numerically many more bubbles in an efficient way (for instance to study modifications of turbulence by bubbles), realistic models of the various forces acting on bubbles are required. It is therefore crucial to know how the drag and lift – or, in non-dimensional form, the drag and lift coefficients – depend on the particular flow situation, i.e. on the local velocity, shear, or vorticity, etc.

The importance and subtlety of the lift force is reflected in various examples. (i) In upward vertical pipe flow, the lateral distribution of bubbles is governed by the lift. The radial bubble migration is found to depend strongly on the bubble size: small bubbles migrate towards the pipe wall, whereas large bubbles tend to accumulate in the centre, resulting in a core-peak bubble distribution (Guet *et al.* 2004). The sign of the lift force is believed to depend also on the bubble's shape. Measurements of lift forces for bubbles in a simple shear flow were carried out at moderate Re by Tomiyama (2002). These measurements indicate negative lift forces for large deformed bubbles, resulting in a lateral motion of the bubbles opposite to that predicted for

a spherical bubble by inviscid theory. (ii) Numerical simulations of bubble-laden homogeneous and isotropic turbulent flow show that the role of the lift force is crucial, because it strongly enhances the preferential accumulation of bubbles in the downward flow side of vortices (Climent & Magnaudet 2006; Mazzitelli, Lohse & Toschi 2003*a*, *b*). This results in a considerably reduced rise velocity of the bubbles and an alteration of large-scale motion.

The aim of this work is to measure experimentally the lift and drag forces in a well-defined flow geometry, with well-defined and temporal constant flow velocity and vorticity. More specifically, we revisit the experiments by Naciri (1992) who studied a bubble in a rotating cylinder, i.e. in a well-defined solid-body rotating flow. The advantage of this set-up is that the bubbles reach a stable position. In this equilibrium position, the forces acting on the bubble – buoyancy, viscous drag, added mass, inertial (or pressure gradient) force and lift – exactly balance each other. Drag and lift can then be deduced from the known added mass, inertial and buoyancy forces. As compared to Naciri (1992), we considerably extended the studied parameter space and also improved the experimental precision. We also compare our results with those from Sridhar & Katz (1995) who studied the force on a bubble crossing a vortex ring.

Related work is described in Rensen *et al.* (2001) where we study the competition between hydrodynamical and acoustical forces and in Lohse & Prosperetti (2003). Complementary work on the analysis of heavy particles in solid-body rotation is reported in Ashmore, del Pino & Mullin (2005) and Seddon & Mullin (2006), where the focus is on the interaction of the heavy object with the wall.

The outline of this paper is as follows. In § 2, the equation of motion of a bubble is introduced, the relevant dimensionless numbers are indicated and previous results for lift and drag coefficients are discussed. The experimental set-up is described in § 3. The results for the drag and lift coefficient measurements are stated in § 4 followed by concluding remarks in § 5.

2. Effective forces on bubbles

2.1. *Dynamical equations, flow field and dimensionless parameters*

For a clean (i.e. uncontaminated by surfactants) spherical bubble rising at moderate-to-large Reynolds number, the approximate force balance is (Magnaudet & Eames 2000):

$$\rho_l V_b C_A \frac{\mathrm{d}\boldsymbol{v}}{\mathrm{d}t} = \rho_l V_b (C_A + 1) \frac{\mathrm{D}\boldsymbol{U}}{\mathrm{D}t} + \rho_l V_b C_L (\boldsymbol{U} - \boldsymbol{v}) \times (\boldsymbol{\nabla} \times \boldsymbol{U}) + \tfrac{1}{2} \rho_l C_D A |\boldsymbol{U} - \boldsymbol{v}| (\boldsymbol{U} - \boldsymbol{v}) - \rho_l V_b \boldsymbol{g}, \quad (2.1)$$

where $\boldsymbol{v}$ is the bubble velocity, $\boldsymbol{g}$ the acceleration due to gravity, ρ_l the liquid density $\gg$ ρ_g the gas density, V_b the bubble volume, and A the projected area of the bubble. $\boldsymbol{U}$ is the velocity of the undisturbed ambient flow taken at the centre of the bubble. This empirical equation is known to hold approximately for $Re > 5$. It depends on three coefficients, two of which are *a priori* unknown: the lift coefficient C_L, and the drag coefficient C_D. The same equation holds for spheroidal bubbles translating about one of their principal axes. For such spheroidal bubbles, C_A is known (Lamb 1934) and becomes 1/2 in the spherical case for all Re (Magnaudet & Eames 2000). Equation (2.1) takes into account added mass, inertia, shear-induced lift, viscous drag and buoyancy. We stress once more that (2.1) is not a good description for

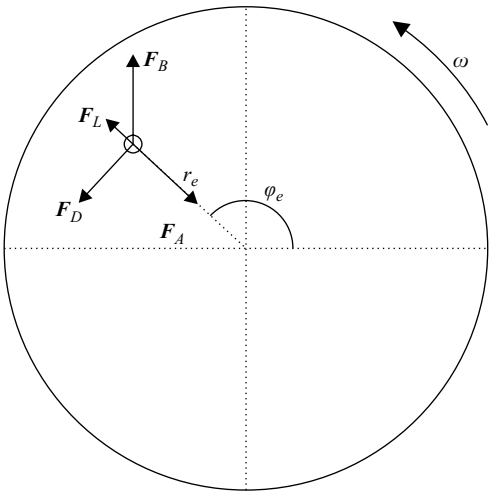

FIGURE 1. Balance of buoyancy, viscous drag, shear-induced lift, pressure gradient and added mass forces. The position of the bubble is given in cylindrical coordinates, in which the rotation and symmetry axis of the cylinder coincide with the z-axis. The cylinder rotates counterclockwise with constant angular velocity ω.

low-Reynolds-number particles, as then the lift contribution is not appropriately parameterized and the history force matters (see e.g. Yang & Leal 1991; Galindo & Gerbeth 1993; Legendre & Magnaudet 1998; Magnaudet & Legendre 1998; Toegel, Luther & Lohse 2006). We will discuss the applicability of (2.1) in more detail in § 2.3.

In a solid-body rotating flow with constant angular velocity ω, see figure 1, the undisturbed flow in cylindrical coordinates is:

$$\boldsymbol{U}(r) = \omega r \hat{\boldsymbol{e}}_\varphi, \tag{2.2}$$

with vorticity $\nabla \times \boldsymbol{U} = 2\omega \hat{\boldsymbol{e}}_z$. The dimensionless numbers characterizing the system are the Reynolds, Strouhal and Froude numbers,

$$Re = \frac{2R_b|\boldsymbol{U}-\boldsymbol{v}|}{\nu}, \qquad Sr = \frac{2R_b\omega}{|\boldsymbol{U}-\boldsymbol{v}|}, \qquad Fr = \frac{|\boldsymbol{U}-\boldsymbol{v}|^2}{2R_b g}. \tag{2.3}$$

Here, R_b is the equivalent bubble radius and ν the kinematic viscosity. Note that the product of the Reynolds and Strouhal numbers results in another 'Reynolds' number, Re_ω, which is just the Taylor number, namely,

$$Re_\omega = Re\,Sr = \frac{(2R_b)^2\omega}{\nu}. \tag{2.4}$$

It is known that the Taylor number is the central dimensionless control parameter of particle dynamics in low-Re rotating flows (Herron, Davis & Bretherton 1975; Gotoh 1990). The Weber number,

$$We = \frac{2R_b\rho_l|\boldsymbol{U}-\boldsymbol{v}|^2}{\sigma}, \tag{2.5}$$

where σ denotes the surface tension, determines whether the bubble will be spherical or not. When $We \ll 1$, the bubble can be assumed to be spherical.

2.2. *Drag force*

For a clean spherical bubble in steady motion in a uniform flow, the viscous drag force may be described by introducing the empirical relation due to Mei, Klausner & Lawrence (1994) for the drag coefficient C_D which matches asymptotic results in the limit of both low and high Re:

$$C_D = \frac{16}{Re}\left[1 + \left[\frac{8}{Re} + \tfrac{1}{2}\left(1 + 3.315Re^{-1/2}\right)\right]^{-1}\right]. \tag{2.6}$$

Owing to contamination of the liquid, surfactants may collect on the bubble surface and the zero-shear-stress boundary condition on the surface may no longer be valid. The viscous drag then increases and, for many surfactants, approaches that of a solid sphere, as indicated (for example) by the measurements by Sridhar & Katz (1995), Maxworthy *et al.* (1996) and Naciri (1992). For a solid sphere, one of the most widely used parameterizations for the drag coefficient is (Clift, Grace & Weber 1978):

$$C_D = \frac{24}{Re}[1 + 0.15Re^{0.687}]. \tag{2.7}$$

Shear effects also increase the viscous drag force by broadening the near wake. Numerical simulations of a bubble in a linear shear flow (Legendre & Magnaudet 1998) reveal a significant dependence of the drag coefficient on the dimensionless shear rate (Sr) for moderate-to-large Re (typically, $Re \geqslant 50$). Whereas the drag remains essentially unaffected for $Sr \leqslant 0.2$, a huge increase is observed for $Sr = O(1)$. From their numerical data, they found the relation:

$$C_{D,Sr} = C_{D0}(1 + 0.55\,Sr^2), \tag{2.8}$$

where C_{D0} is the drag coefficient in the absence of shear.

2.3. *Lift force*

There have been various theoretical and numerical investigations of the lift force experienced by rigid spheres and bubbles in vortical flows. For a quasi-steady weak (i.e. $Sr \ll 1$) linear shear flow, Auton (1987) analytically predicted the lift coefficient involved in (2.1) to be $1/2$ in the inviscid limit. Auton, Hunt & Prud'Homme (1988) combined this result with that of Taylor (1928) for the force on a sphere in an unsteady strained flow. In the limit of weak vorticity and unsteadiness, they showed that Auton's (1987) result may simply be added to Taylor's (1928) result, yielding the inviscid part of (2.1).

As pointed out above, an experiment similar to the present one was carried out by Naciri (1992). He found experimentally that the lift coefficient depended on the Froude number for $0.3 < Fr < 2.6$ and parameterized this dependence as:

$$C_L^N = \tfrac{1}{2}(1 + C_A) - \frac{0.81}{\sqrt{Fr}} + \frac{0.29}{Fr}. \tag{2.9}$$

The superscript N stands for Naciri. The range of Reynolds numbers covered in these measurements is between 10 and 2500, and the bubble radii ranged from 0.4 to 6 mm.

Similarly, Sridhar & Katz (1995) studied bubbles entrained in vortices produced by a vortex ring generator. This is not solid-body rotation, because vorticity decays away from the core. Moreover, the authors used tap water, so their bubbles were contaminated by surfactants. The measured lift coefficients were found to be almost independent of the Reynolds number, but dependent on the shear rate through the

following empirical relation:

$$C_L^{SK} = 0.22\, Sr^{-0.75}, \tag{2.10}$$

for $20 < Re < 80$, $0.004 < Sr < 0.09$ and bubble radii ranging from 0.25 to 0.4 mm. The measured lift coefficients were substantially larger than theoretical predictions, which is not surprising since the low- (resp. high-) Re results were compared with Saffman's (1965) result (resp. with Auton's (1987) result), both of which were derived for a pure shear flow. Other empirical correlations are based on numerical simulations of the detailed flow structure around a sphere. Bagchi & Balachandar (2002) studied vortex-induced lift for a rigid sphere at moderate Re in the range 10 to 100 and weak vorticity ($0.04 < Sr < 0.1$). They found a significantly enhanced positive lift coefficient for vortex flows in agreement with the measurements of Sridhar & Katz (1995) and again at odds with predictions from inviscid and low-Re theories.

In a solid-body rotating flow with constant angular velocity ω, both the shear-induced lift force ($\boldsymbol{F}_L$) and the added mass and inertial force ($\boldsymbol{F}_A$) acting on a bubble in equilibrium have only radial components, and can be combined in terms of a rotational lift force. In the inviscid limit, this yields for a bubble at rest

$$\begin{aligned}\boldsymbol{F}_L + \boldsymbol{F}_A &= \rho_l V_b \left[C_L \boldsymbol{U} \times (2\omega \hat{\boldsymbol{e}}_z) + (C_A + 1)\frac{\mathrm{D}\boldsymbol{U}}{\mathrm{D}t} \right] \\ &= \rho_l V_b \omega^2 r_e [2C_L - (C_A + 1)]\, \hat{\boldsymbol{e}}_r = 2C_{L\Omega} \rho_l V_b \omega^2 r_e\, \hat{\boldsymbol{e}}_r, \end{aligned} \tag{2.11}$$

where r_e is the equilibrium radial position of the bubble (see figure 1) and the rotational lift coefficient is defined as:

$$C_{L\Omega} = C_L - \tfrac{1}{2}(1 + C_A), \tag{2.12}$$

For a sphere, (2.12) results in $C_{L\Omega} = -1/4$, indicating that the direction of the total lift force is opposed to that found in a simple shear flow. This is because the inertial and added-mass forces (which are strictly zero in a linear shear flow) are centripetal in a solid-body rotation flow and exceed the centrifugal shear-induced lift force. Magnaudet & Legendre (1998) obtained an empirical expression from numerical simulations for the rotational lift coefficient for a spherical shear-free bubble in solid-body rotation for $10 < Re < 1000$ and for weak to moderate shear ($0.02 < Sr < 0.2$), namely

$$C_{L\Omega}^{ML} = -0.25 + 1.2\, Re^{-1/3} - 6.5\, Re^{-1} + O(Re^{-1}). \tag{2.13}$$

Although (2.1) is widely used to track bubbles over a wide range of Reynolds numbers, it must be realized that it is inadequate in the low-Re regime. For instance, in the flow considered here, the inertial and added-mass contributions provided by the fluid acceleration are $O(ReSr)$ (adopting a scaling in which the viscous drag is $O(1)$), so that they are negligibly small compared to contributions such as the history force which is neglected in (2.1). More importantly, the expression of the shear-induced lift force involved in (2.1) (the second term on the right-hand side) is specific to moderate or large Re. In contrast to this $O(ReSr)$ lift contribution, low-Re shear-induced lift forces are $O((ReSr)^{1/2})$, as first shown by Saffman (1965). Hence, they provide the dominant hydrodynamic contribution to the radial force balance. The low- and high-Re scalings of the shear-induced lift force are different because the underlying physics differ from each other. At large Reynolds number, the shear-induced lift force taken into account in (2.1) results from the tilting of the upstream vorticity around the bubble which is a body of finite span, like an airfoil. This tilting induces a non-zero streamwise component of the vorticity in the wake,

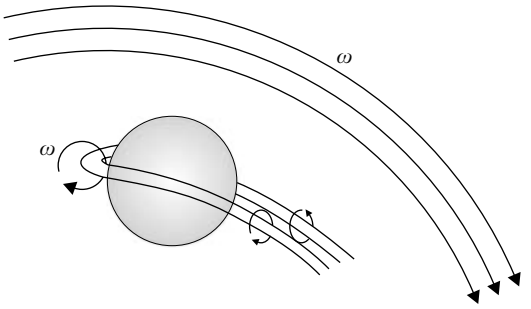

FIGURE 2. Sketch of the shear-induced lift mechanism in the high-*Re* regime. The vortex pair behind the bubble induces a lift force.

which gives rise to a pair of counter-rotating vortices (figure 2). The flow created by this pair of vortices results in a force $\boldsymbol{F}_L$ which, in a pure linear shear flow as well as in the solid-body rotation considered here, tends to push the body towards the high relative velocity side (as pointed out earlier, besides this shear-induced force there is in general another contribution to the lift which is due to the fluid acceleration $\mathrm{D}\boldsymbol{U}/\mathrm{D}t$, and which in the present flow is dominant and makes the total lift force centripetal).

In contrast, the low-*Re* picture relies on the far-field flow in which the disturbance produced by the body (i.e. the force due to the Stokeslet associated with the body) generates small inertial and viscous contributions of similar magnitude, which in turn produce a small uniform flow in the vicinity of the body. The direction of this uniform flow is generally not aligned with that of the primary flow, resulting in a lift force. For a bubble or a rigid sphere moving along a simple shear flow, this force has the same direction as its high-*Re* counterpart, but the two mechanisms differ. At low Reynolds number, the sign of the force results from the displacement of fluid particles in the far-wake relative to the ambient flow, which increases (if the particle is fixed) in the direction of increasing velocities, resulting in a lateral pressure gradient which tends to move the particle in the same direction. This was the situation considered in the pioneering work of Saffman. While determining the sign of the low-*Re* lift force on the grounds of simple physical arguments is relatively easy in this case, it is frequently less intuitive when the particle moves at an arbitrary angle to the base flow, or when the latter is not unidirectional. In the situation we are considering here, two opposite effects are competing. First, given the linear increase of the undisturbed velocity with the local radius r, the velocity difference between the outer (undisturbed) flow and the defect velocity within the wake is larger on the outward side of the wake than on the inner side. This effect, similar to that encountered with a fixed particle embedded in a pure shear flow, results in a centrifugal lift force ($\boldsymbol{F}_{L1}$ in figure 3). On the other hand, it must be borne in mind that the wake centreline approximately follows the streamlines of the base flow, i.e. the wake is curved by the external flow. Then, considering that any slice of wake results in an infinitesimal force $\delta\boldsymbol{F}_w$ perpendicular to its plane and directed downstream, it is immediately seen in figure 3 that the total wake-induced force $\boldsymbol{F}_w = \int \delta\boldsymbol{F}_w$ obtained by integrating along the wake consists of a drag force and a centripetal contribution ($\boldsymbol{F}_{L2}$ in figure 3). The question is then which of the centrifugal and centripetal lift contributions, both of which are $O((ReSr)^{1/2})$, is larger. There seems to be no rational way to settle this question on the basis of simple qualitative arguments. However, the full theoretical determination of the corresponding transverse force for a fixed sphere embedded in a solid-body

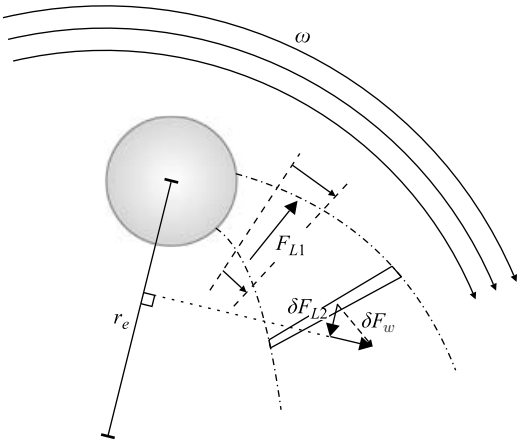

FIGURE 3. Sketch of the lift mechanism in the low-*Re* regime. There are two opposite contributions $\boldsymbol{F}_{L1}$ and $\boldsymbol{F}_{L2}$ to the lift force. For a detailed description of the mechanism see the end of § 2.3.

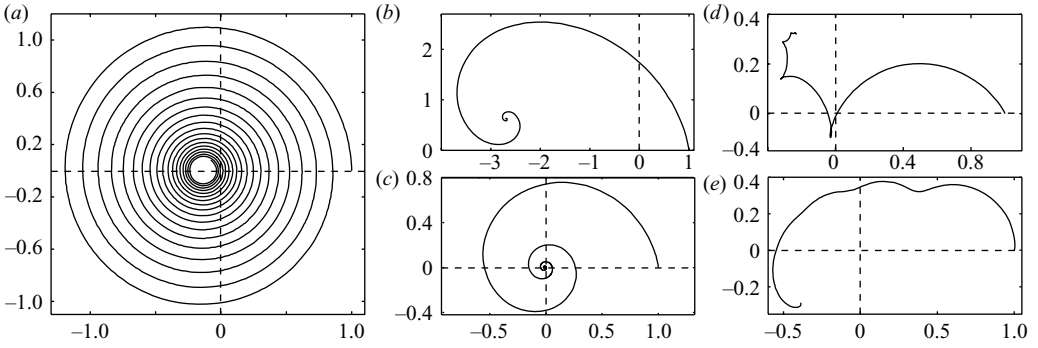

FIGURE 4. Theoretical bubble trajectories for different values of Re_ω and C_L: (*a*) spiral with $Re_\omega = 0.1$, (*b*) spiral with $Re_\omega = 1$, (*c*) spiral with $Re_\omega = 10$, (*d*) cycloid with $Re_\omega = 50$ and (*e*) non-spiral with $Re_\omega = 50$. In (*a*)–(*d*) $C_L = 0.5$, while in (*e*) $C_L = 0.9$; $R_b = 0.5$ mm in all cases. The bubble was released from (1, 0) each time, both x and y axes are in mm.

rotation flow was achieved by Gotoh (1990) under asymptotic conditions identical to those considered by Saffman (1965). His result indicates that the centripetal effect is dominant, which implies that the lift coefficient is negative if the force is expressed using the inertial scaling of (2.1). The prefactor of this $O((ReSr)^{1/2})$ centripetal force is about six times smaller than that of the Saffman shear-induced lift force, a reduction which may be interpreted as a direct consequence of the competition between the two opposite contributions $\boldsymbol{F}_{L1}$ and $\boldsymbol{F}_{L2}$. The most important conclusion we can draw from the above considerations is that the mechanisms responsible for the shear-induced lift force are deeply different in the high- and low-*Re* regime. In the particular case of a fixed sphere embedded in a solid-body rotation flow, we expect this force to change from centrifugal to centripetal as the Reynolds number is decreased.

2.4. *Trajectories and equilibrium bubble position*

We now show typical bubble trajectories as they follow from the dynamical equation (2.1) with assumed drag and lift coefficients. Figure 4 shows the trajectory of the bubble for different values of $Re_\omega = (2R_b)^2\omega/\nu$ and C_L. To calculate these theoretical

trajectories, C_A was assumed to be 1/2 and (2.7) was used for C_D. For higher Re_ω and C_L (figure 4*d*, *e*), the trajectories tend to go from spiralling towards cycloidal motion.

Finally, the bubble will reach an equilibrium position (r_e, φ_e) where all forces acting on it balance, as shown in figure 1. The axial position is kept fixed, as for small enough bubbles, there is no axial asymmetry capable of inducing forces acting in the axial direction. Note that for large bubbles in the $R_b \sim 1$ cm regime, this can change (Bluemink *et al.* 2005). From the equation of motion (2.1), we therefore have two balance equations – one in the radial and one in the azimuthal direction – which for the equilibrium situation $\dot{r} = \ddot{r} = \dot{\varphi} = \ddot{\varphi} = 0$ can be solved for r_e and φ_e,

$$\tan\varphi_e = \frac{8}{3}\frac{R_b}{C_D r_e}(2C_L - 1 - C_A), \tag{2.14}$$

$$r_e = \frac{-g\sin\varphi_e}{\omega^2(2C_L - 1 - C_A)}. \tag{2.15}$$

Here, the flow field from (2.2) has been used. The final position of the bubble (r_e, φ_e) depends on ω, R_b, ρ_l, g, and on the kinematic viscosity of the fluid ν (since it influences the values of C_D and C_L). Vice versa, the equilibrium position (r_e, φ_e) of the bubble directly reveals the lift coefficient C_L and the drag coefficient C_D,

$$C_L = \tfrac{1}{2}\left[1 + C_A - \frac{g\sin\varphi_e}{r_e\omega^2}\right], \tag{2.16}$$

$$C_D = -\frac{8}{3}\frac{R_b}{r_e^2\omega^2} g\cos\varphi_e. \tag{2.17}$$

R_b, ω and ν are the variables that can be adjusted in the experiment. The response of the system is reflected in the equilibrium position (r_e, φ_e) (figure 1), characterized by $\boldsymbol{v} = 0$. The equilibrium radius can be expressed in the dimensionless numbers of (2.3) and (2.5), namely,

$$Re = \frac{2R_b\omega r_e}{\nu}, \qquad Sr = \frac{2R_b}{r_e}, \qquad Fr = \frac{\omega^2 {r_e}^2}{2R_b g}, \qquad We = \frac{2R_b\rho_l\omega^2 r_e^2}{\sigma}. \tag{2.18}$$

In both simulations and experiments, we find that the bubble equilibrium position is stable. Experimentally we test the stability by disturbing the bubble at equilibrium with another bubble of similar size. Once that second bubble approaches the bubble at equilibrium, the first bubble is kicked out of the equilibrium position, but then re-approaches it again. To further support the stability of the equilibrium position, a linear stability analysis was done for (r_e, φ_e) in (2.1), indeed confirming stability as long as $\rho_l > \rho_b$.

3. Experiment

3.1. *Set-up, uncertainties and data analysis*

The experimental apparatus is sketched in figure 5. A glass cylinder of 500 mm length and 100 mm inner diameter, is filled with de-ionized water or a water–glycerin mixture and is rotated with an angular velocity ω in the range of 2–35 rad s^{-1} $\pm$ 0.5 % (at high rotation rates mechanical vibrations introduce additional errors). A bubble is injected approximately midway along the cylinder. The bubble size is controlled such that R_b is typically around 1 mm (uncertainty $\pm$ 2 %), corresponding to $We \ll 1$ in the glycerin/water mixtures and $We \lesssim 1$ in water, so that the bubble is essentially

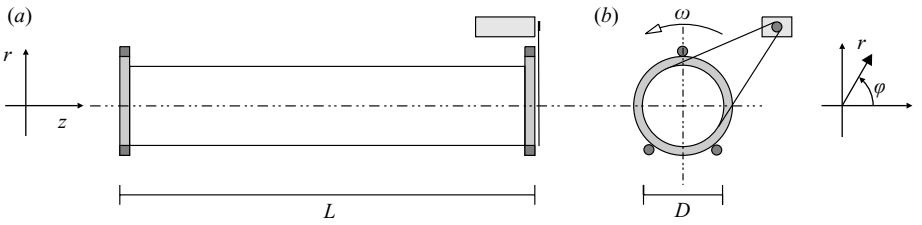

FIGURE 5. Sketch of the experimental set-up. (*a*) Side view: glass cylinder of length $L = 500$ mm. The cylinder axis is aligned with the z-axis of the coordinate system. (*b*) Axial view: the cylinder has diameter $D = 100$ mm. The end caps rest on ball bearings. A d.c. motor drives the cylinder on the right-hand end cap via a toothed belt at constant rotation rate ω.

spherical. The transient motion of the bubble and its equilibrium position are recorded with a digital camera.

By image processing, the equilibrium position of the bubble (r_e, φ_e) is obtained, and from this, *Re* and *Sr* are determined. The experiments were conducted with *Re* in the range 10^{-2}–10^3 and *Sr* varying between 0.1 and 2. As the rotation rate is decreased, the equilibrium radius r_e increases. Therefore, there is a lower limitation on ω in order to avoid wall effects. In general, for low-*Re* and high rotation rates, equilibrium positions are close to the rotation axis and therefore accompanied by low accuracy of the r_e and φ_e measurements. Considerable effort was made to reduce the experimental errors and uncertainties to a minimum for these low-*Re* experiments. In order to have a reliable measurement of the equilibrium position, the camera was placed on a two-way rotatable, $x - y - z$ translation stage to align the optical axis as precisely as possible with the axis of rotation of the cylinder. Additionally, the location of the rotation axis in the digital images was determined by linear extrapolation of the centre-positions on the front and back end of the cylinder. Image analysis demonstrated a final uncertainty in the x, y position of the bubble centre of no more than 0.75 pixels. Finally, the uncertainty in r_e was between 3 and 7 %, and the uncertainty in φ_e was between 0.1° and 4°, depending on the final bubble position.

For the water–glycerin mixtures, the viscosity ν and density ρ_l were measured using standard equipment, and the resulting accuracies are ± 5 % and ± 0.1 %, respectively. The accuracy of the surface tension σ was estimated to be 0.5 %. The systematic uncertainties of compounded quantities (such as *Re*, *Sr*, etc.) were determined from the systematic component uncertainties by the standard error propagation method. For the case of *Sr* this, for example, leads to $\Delta Sr/Sr = \Delta R_b/R_b + \Delta r_e/r_e$, implying that the uncertainties in *Sr* range from 5 to 9 %.

Image sequences are typically recorded at 500 frames per second. The effect of inhomogeneous background illumination is removed by subtracting an empty background image, after which a global grey-level threshold is applied for image segmentation. For each frame in the image sequence, the position of the cylinder centre, that of the centroid of the bubble and the length of its major and minor axes are computed.

3.2. *Sphericity of bubbles and flow-field uniformity*

For 60 out of 78 recorded bubbles, the aspect ratio (major/minor axis $= \chi$) was below 1.1. Data points for which the shape was less spherical (i.e. points corresponding to bubbles with an aspect ratio larger than 1.1) are indicated as such in the figures. The largest observed aspect ratio was 1.66 (for a bubble with $R_b = 1$ mm, $Re = 622$ and

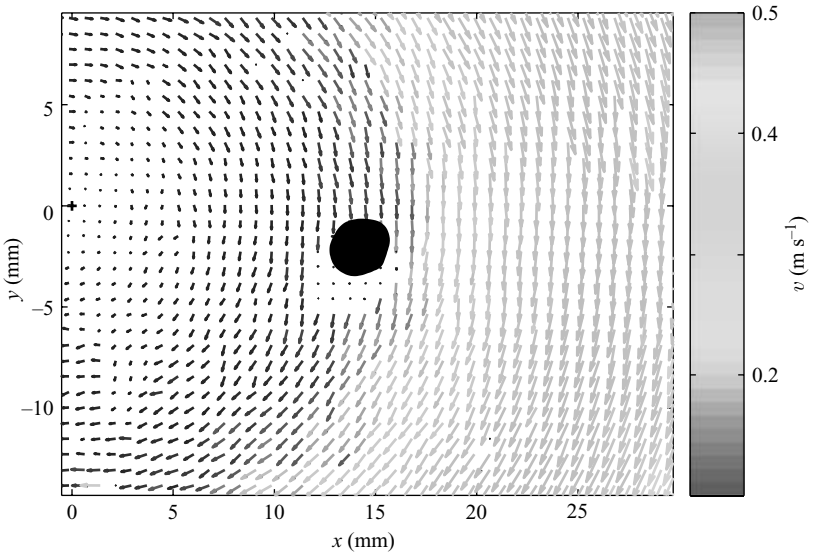

FIGURE 6. Flow field around a large bubble ($R_b \approx 1.5$ mm) at equilibrium, as measured by particle image velocimetry (PIV). Note how the influence of the bubble is negligible just a few bubble diameters downstream. In this case, $Sr = 0.21$, $Re = 585$. PIV images for further cases with different Sr and Re and more details on the method can be found in Bluemink *et al.* (2005).

$\omega = 34.9$). Note that the aspect ratio of the bubbles (oblate spheroids) is taken into account when calculating C_A (Lamb 1934) and hence (through (2.16) and (2.17)) C_L etc. For $\chi = 1.1$, we obtain $C_A = 0.56$, an increase of about 10 % as compared to the spherical case.

The approximate sphericity of the bubbles is confirmed by formally calculating the Weber number according to (2.18). Indeed, all of the bubbles considered in the present analysis have $We \leqslant 2.66$; the average Weber number is only 0.54. The bubble with the largest Weber number, $We = 2.66$, also has the largest measured aspect ratio, namely 1.66. Results for larger bubbles are given in Bluemink *et al.* (2005); for these large bubbles, the phenomenology is rather different as they deform to such a degree that off-diagonal elements of the added mass tensor become relevant, leading to a motion of the bubble along the axis of the cylinder.

The quality of the flow field and the influence of the wake behind the bubbles on their equilibrium position were studied using particle imaging velocimetry (PIV). As can be seen in figure 6, even for a relatively large bubble, the wake quickly decays and does not seem to affect the incident flow on the bubble. Therefore, we consider it reasonable to assume that the flow field is in a state of uniform solid-body rotation. Also, order of magnitude estimates indicate that the wake should be negligible for $Sr < 1$. In our current data, Sr is smaller than 3 for all bubbles and only for 8 bubbles is it between 1 and 3.

4. Experimental results for bubbles in vortical flow

4.1. *Trajectories*

Figure 7 shows typical experimental trajectories for Reynolds numbers in the range from 102 to 622. Figures 7(*a*) and 7(*b*) show spirals; the lower the angular velocity,

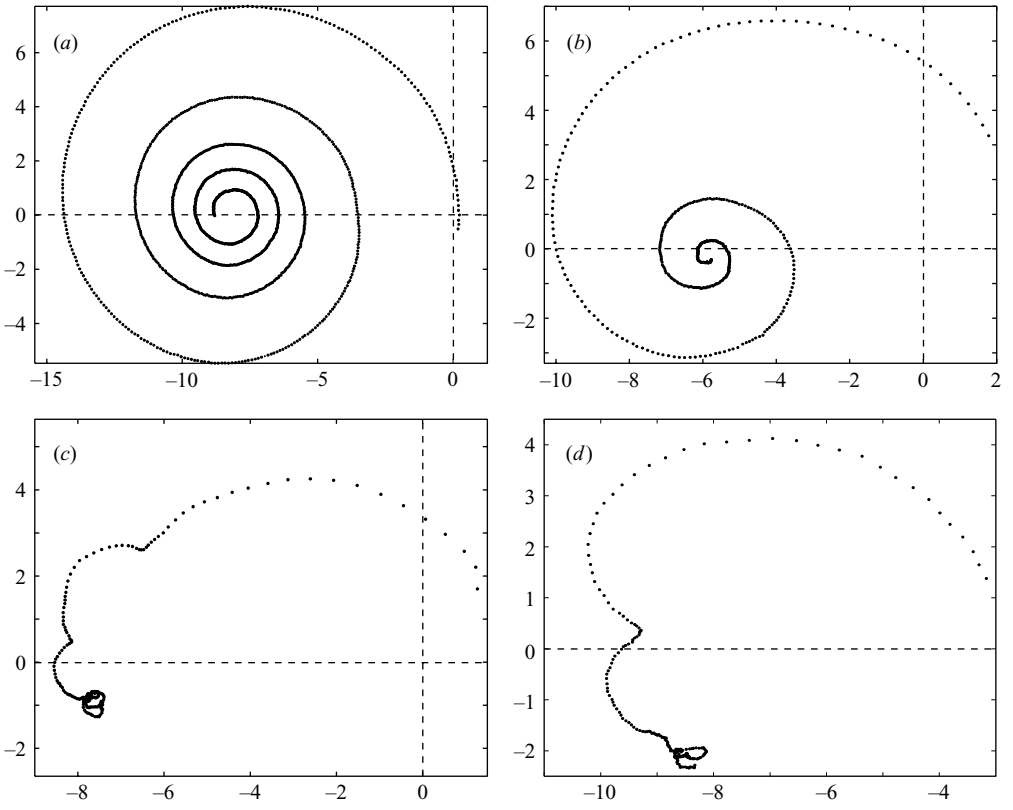

FIGURE 7. Typical experimental trajectories of the bubble: (*a*) $Re = 102$, $\omega = 15\,\mathrm{rad\,s^{-1}}$, $R_b = 0.4\,\mathrm{mm}$, $Re_\omega = 10$; (*b*) $Re = 186$, $\omega = 23.3\,\mathrm{rad\,s^{-1}}$, $R_b = 0.7\,\mathrm{mm}$, $Re_\omega = 45$; (*c*) $Re = 400$, $\omega = 35\,\mathrm{rad\,s^{-1}}$, $R_b = 0.7\,\mathrm{mm}$, $Re_\omega = 69$; (*d*) $Re = 622$, $\omega = 35\,\mathrm{rad\,s^{-1}}$, $R_b = 1.0\,\mathrm{mm}$, $Re_\omega = 140$. Both axes are in mm, and the centre of the cylinder corresponds to $x = 0$, $y = 0$.

the more slowly the bubble moves inwards, leading to a more closely wound spiral. In other words, increasing the shear rate on the bubble reduces the entrapment time. Also, as *Sr* increases, the equilibrium position shifts towards the cylinder centre. As both *Re* and *Sr* increase, the trajectories become more complex and resemble cycloids (figure 7*c*, *d*). Once the bubble has reached the vicinity of the equilibrium position, it seems to be captured on an erratic trajectory. We interpret this motion as jitter due to lack of stability in ω and in the horizontal alignment of the system. Note that both spiralling and cycloidal motions are found in experiments (figure 7) as well as in simulations (figure 4). For both, we find that cycloidal motion is predominant for large *Re* and/or *Sr*. Attempts were made to integrate (2.1) numerically using experimental data as input, thus providing a direct comparison between numerics and experiment. The agreement between the numerical integration and experiment was reasonable at best, indicating that the models for $C_L(Re, Sr)$ input into the numerical integration are not accurate enough. Additional problems in these comparisons arise because 'real' bubbles have a finite eccentricity which introduces added mass components parallel to the direction of bubble motion, not accounted for in the numerical simulations. In § 5, we re-address the difficulty of numerically reconstructing the whole bubble trajectory.

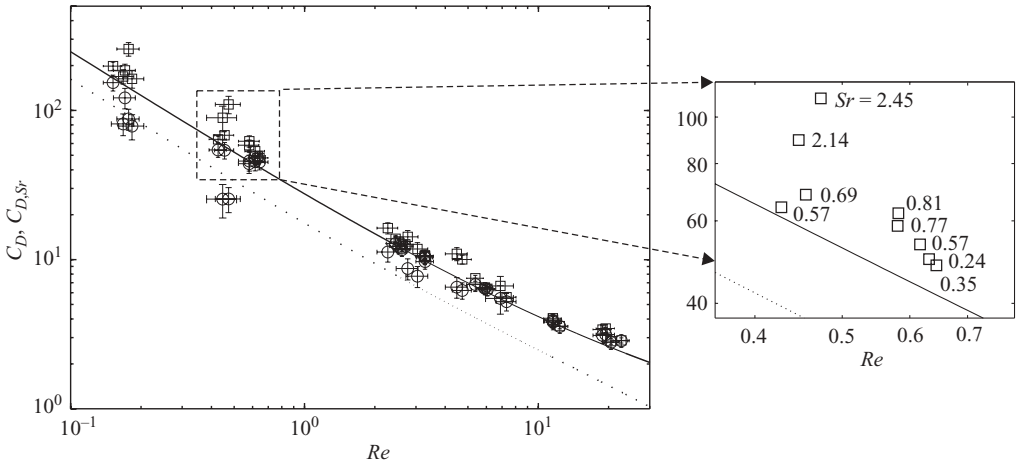

FIGURE 8. Drag coefficient versus Reynolds number. The drag coefficients C_D are indicated by squares. The corresponding circles indicate the coefficients $C_{D,Sr}$ with shear correction according to (2.8). The solid line represents the drag coefficient for solid spheres, (2.7). The dashed line is for clean spherical bubbles according to (2.6).

4.2. *Equilibrium positions*

4.2.1. *Drag coefficient*

Figure 8 shows the measured dependence of the drag coefficient C_D on the Reynolds number, as calculated from the equilibrium position (cf. (2.17)). Additionally, the drag curves for a clean spherical bubble (2.6) and a solid sphere (2.7) in a uniform flow are shown. We would expect the drag coefficients to fall between the two lines, indicating a certain amount of contamination of the system. However, the measured drag coefficients (open symbols in figure 8) are systematically above the solid drag curve. As indicated by the error bars, measurement errors cannot explain this effect. Taking a closer look at Sr for the different data points reveals that the deviation from the solid drag curve is larger when Sr is larger. Assuming that the drag coefficient depends on the shear rate as given in (2.8), the measured $C_{D,Sr}$ coefficients can be shear-compensated, i.e. we can estimate the drag coefficient C_{D0} that the bubble would have if it were embedded in a uniform flow. The result of such a compensation is shown in figure 8 (closed symbols); compensated drag coefficients tend to fall in between the drag curves for a clean spherical bubble and a solid sphere, indicating that the shear on a particle embedded in solid-body rotation modifies the drag in a qualitatively similar fashion as in a linear shear flow.

4.2.2. *Lift coefficient*

Figure 9 shows the dependence of the lift coefficient on Sr, over three decades of Sr. In this plot we compare our results with available data from Sridhar & Katz (1995) and Naciri (1992). There is some discrepancy between our measurements and Sridhar & Katz's extrapolated fit, but this discrepancy decreases with increasing Re.

Figure 10 shows the available data versus $Fr^{1/2}$. It summarizes the measurements of Naciri and our data in glycerin–water mixtures and water. The empirical fit suggested by Naciri does not hold for our data, and hence the Froude number does not seem to be an adequate parameter to describe our results.

Figure 11 shows the dependence of the lift coefficient on Re. While Sridhar & Katz (1995) noted that their data for C_L did not seem to depend on Re, our measurements

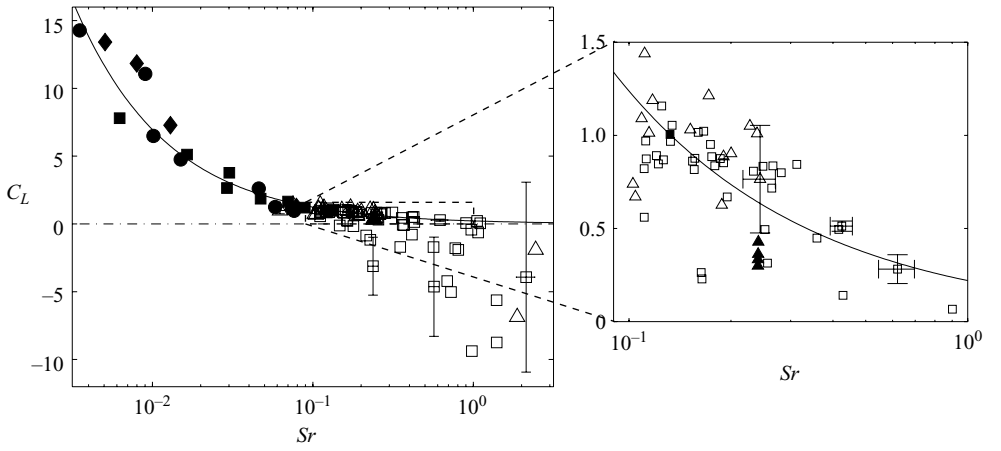

FIGURE 9. Lift coefficient C_L versus Strouhal number Sr: our data sets with a bubble aspect ratio $\chi > 1.1$ (△) and with $\chi < 1.1$ (□), Sridhar & Katz's data (■: $20 < Re < 30$, ●: $50 < Re < 70$, ◆: $65 < Re < 80$), and Naciri's data (▲, taken from Sridhar & Katz 1995). Superposed is the empirical model suggested by Sridhar & Katz (equation (2.10), solid line). The inset shows the spread of our data more clearly, including some typical error bars.

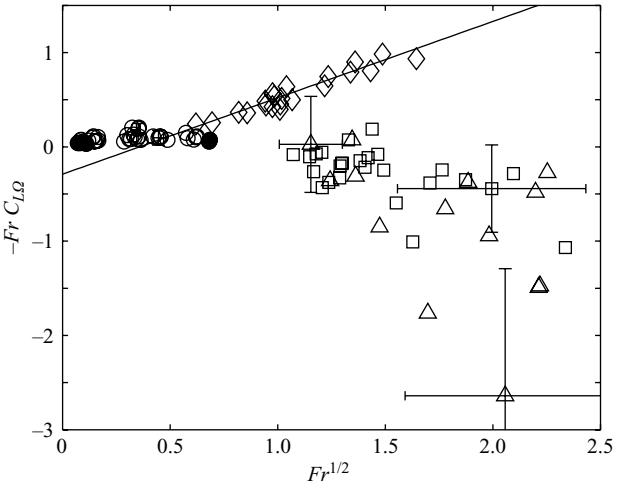

FIGURE 10. $-Fr\,C_{L\Omega}$ versus $Fr^{1/2}$: glycerine–water results (○ for a bubble aspect ratio $\chi < 1.1$ and ● for $\chi > 1.1$), results for water (□ and △ for $\chi < 1.1$ and $\chi > 1.1$, respectively) and Naciri's results (◇) taken from figure II.6 in Naciri (1992). Superposed is the empirical fit suggested by Naciri (2.9), which cannot describe the present data.

indicate a strong dependence on Re at low Re. Moreover, the shear-induced lift coefficient C_L is found to be negative for $Re < 5$ (an Re range in which Sridhar & Katz did not measure C_L), as the rotational lift coefficient $C_{L\Omega} < -3/4$ in this range (cf. (2.12)). Figure 11 contains data from our experiments (triangles and squares) and numerical data (circles) obtained by Magnaudet & Legendre (1998). For $Re > 5$, both the experiments and the simulations are in good agreement with the high-Re theoretical prediction. In particular, for large Re, they both converge to the asymptotic value of $C_{L\Omega} = -1/4$ corresponding to $C_L = 1/2$. For $Re < 5$, the numerical results show a strongly decreasing trend for C_L which becomes negative for small enough

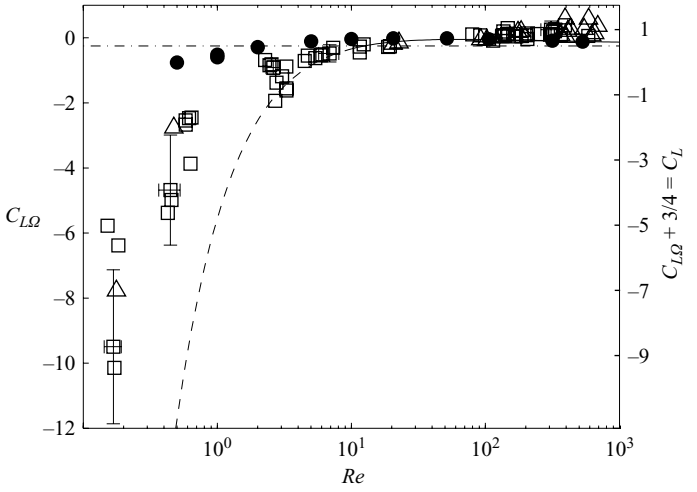

FIGURE 11. Rotational lift coefficient $C_{L\Omega}$ versus Reynolds number Re. The measured rotational lift coefficients $C_{L\Omega}$ and typical error bars are indicated by □ and △ for $\chi < 1.1$ and $\chi > 1.1$, respectively. The solid circles are results of numerical simulations from Magnaudet & Legendre (1998). The dot-dashed line is the asymptotic value $C_{L\Omega} = -1/4$ for $Re \to \infty$. The solid line (for $Re > 10$) and dotted line (for $Re < 10$) come from (2.13) which is valid for $Re \geqslant 10$. The right-hand axis shows the corresponding lift coefficient C_L, calculated with the assumption that $C_A = 1/2$.

Re. The experimental data show a similar but even more pronounced trend, the shear-induced lift coefficients becoming negative when $Re < 5$. Hence, it appears that the transition between the high-Re and low-Re mechanisms for the generation of the shear-induced lift force discussed in § 2.3 occurs around $Re = 5$. Magnaudet & Legendre (1998) observed the same trend in a linear shear flow. More precisely, they found the low-Re scaling involved in Saffman's (1965) and McLaughlin's (1991) predictions to apply for $Re < 2$, approximately, and the two regimes to match around $Re = 5$.

According to the low-Re theory, $C_{L\Omega}$ should be proportional to $(ReSr)^{-1/2}$ in the corresponding regime, provided $(Sr/Re)^{1/2}$ is much larger than unity (Herron *et al.* 1975; Gotoh 1990). However, our experimental values for the quantity $C_{L\Omega}(ReSr)^{1/2}$ in the range $Re < 5$ are not constant and still decrease significantly as Re goes to zero. This may be because the ratio Sr/Re is not large enough in several cases or may be due to the influence of the bubble wake, keeping in mind that r_e tends to zero with Re so that the incident flow 'seen' by the bubble is not strictly in solid-body rotation. Finally, the experimental accuracy on r_e and φ_e may also be questioned in this regime. We plan to perform new experiments in this regime to clarify this point.

5. Conclusion

In conclusion, the motion of a single bubble in a solid-body rotational flow was studied experimentally. Drag and lift coefficients have been obtained from the measured equilibrium position of the bubble. The dependence of the drag and lift coefficients on shear rate and Reynolds number has been studied over a wide range of Sr and Re. The two main findings of this paper are: (i) there is a significant shear dependence of the drag coefficient for strong shear and (ii) there is a remarkable change of sign in the lift force in solid-body rotation around $Re = 5$. The

aforementioned strong shear dependence of C_D is in agreement with previous numerical predictions by Legendre & Magnaudet (1998). Even though their prediction was made for linear shear flow, it seems to be valid for the case of solid-body rotation also. We find a significant dependence of the lift coefficient on *Sr* and *Re*, especially for strong shear and small *Re*. For $Re > 5$, we find that the total (rotational) lift coefficient $C_{L\Omega}$ is negative, but its values are larger than $-3/4$, yielding positive values of the shear-induced lift coefficient C_L. This is in agreement with predictions from inviscid theory (Auton 1987). In contrast, for $Re < 5$, our experiments show negative shear-induced lift coefficients. That the lift force on a fixed sphere (solid particle or bubble) embedded in a solid-body rotation flow is negative (i.e. centripetal) at low Reynolds number is in line with Gotoh's (1990) theoretical prediction which is the counterpart of Saffman's prediction for the flow configuration considered here. Further improvements of the experimental set-up will allow us to achieve more precise measurements in this low-*Re* range; but note again that (2.1) is not necessarily a good approximation for that low-*Re* regime: First, the history force has been omitted and secondly, the lift force parameterization is inappropriate for small *Re*.

What would be desirable is to reconstruct the whole bubble trajectory with the help of (2.1) and the values obtained for the lift and drag coefficients from our analysis of the equilibrium position. At present, there is no way to achieve this. The accuracy in C_L and C_D is simply not sufficient and additional terms in (2.1) may also play a role. In addition, in a non-stationary situation, the bubble's wake and hence the forces may differ from their steady counterparts. In the numerical simulations these small imperfections accumulate during the spiralling process towards the equilibrium which can take minutes. Therefore, only a local comparison of the bubble trajectories or a comparison between bubble trajectory characters gives satisfactory agreement between experiment and numerics.

S. L. acknowledges support from the European Union (EU) through the European Research Network on 'Nonideal Turbulence' (contract HPRN-CT-200000162). We would like to thank G.-W. Bruggert and H. Scholten for help with the experimental set-up and C. W. Visser for helpful discussions. Many thanks to Michel Duits and the Physics of Complex Fluids group for support with the viscosity measurements. This work is part of the research programme of Stichting FOM, which is financially supported by NWO.

REFERENCES

Ashmore, J., del Pino, C. & Mullin, T. 2005 Cavitation in a lubrication flow between a moving sphere and a boundary. *Phys. Rev. Lett.* **94**, 124501.

Auton, T. 1987 The lift force on a spherical body in a rotational flow. *J. Fluid Mech.* **183**, 199–218.

Auton, T., Hunt, J. & Prud'Homme, M. 1988 The force exterted on a body in inviscid unsteady non-uniform rotational flow. *J. Fluid Mech.* **197**, 241–257.

Bagchi, P. & Balachandar, S. 2002 Shear versus vortex-induced lift force on a rigid sphere at moderate *Re*. *J. Fluid Mech.* **473**, 379–388.

Bluemink, J. J., van Nierop, E. A., Luther, S., Deen, N. G., Magnaudet, J., Prosperetti, A. & Lohse, D. 2005 Asymmetry-induced particle drift in a rotating flow. *Phys. Fluids* **17**, 072106.

Clift, R., Grace, J. R. & Weber, M. E. 1978 *Bubbles, Drops and Particles*. Academic.

Climent, E. & Magnaudet, J. 2006 Dynamics of a two-dimensional up flowing mixing layer seeded with bubbles. Bubble dispersion and effect of two-way coupling, *Phys. Fluids* **18**, 103304.

Galindo, V. & Gerbeth, G. 1993 A note on the force on an accelerating spherical drop at low-Reynolds number. *Phys. Fluids* A **5**, 3290–3292.

Gotoh, T. 1990 Brownian motion in a rotating flow. *J. Stat. Phys.* **59**, 371–402.

Guet, S., Ooms, G., Oliemans, R. & Mudde, R. 2004 Bubble size effect on low liquid input drift-flux parameters. *Chem. Engng Sci.* **59**, 3315–3329.

Herron, I., Davis, S. & Bretherton, F. 1975 On the sedimentation of a sphere in a centrifuge. *J. Fluid Mech.* **68**, 209–234.

Lamb, H. 1934 *Hydrodynamics*, 6th edn. Dover.

Legendre, D. & Magnaudet, J. 1998 The lift force on a spherical bubble in a viscous linear shear flow. *J. Fluid Mech.* **368**, 81–126.

Lohse, D. & Prosperetti, A. 2003 Controlling bubbles. *J. Phys. Condens. Matter* **15**, S415.

McLaughlin, J. B. 1991 Inertial migration of a small sphere in linear shear flows. *J. Fluid Mech.* **224**, 261–274.

Magnaudet, J. & Eames, I. 2000 The motion of high-Reynolds number bubbles in inhomogeneous flows. *Annu. Rev. Fluid Mech.* **32**, 659–708.

Magnaudet, J. & Legendre, D. 1998 Some aspects of the lift force on a spherical bubble. *Appl. Sci. Res.* **58**, 441–461.

Maxworthy, T., Gnann, C., Kürten, M. & Durst, F. 1996 Experiments on the rise of air bubbles in clean viscous liquids. *J. Fluid Mech.* **321**, 421.

Mazzitelli, I., Lohse, D. & Toschi, F. 2003*a* The effect of microbubbles on developed turbulence. *Phys. Fluids* **15**, L5–L8.

Mazzitelli, I., Lohse, D. & Toschi, F. 2003*b* On the relevance of the lift force in bubbly turbulence. *J. Fluid Mech.* **488**, 283–313.

Mei, R., Klausner, J. & Lawrence, C. 1994 A note on the history force on a spherical bubble at finite Reynolds number. *Phys. Fluids* **6**, 418–420.

Naciri, M. A. 1992 Contribution à l'étude des forces exercées par un liquide sur une bulle de gaz: portance, masse ajoutée et interactions hydrodynamiques. PhD thesis, Ecole Central de Lyon.

Rensen, J., Bosman, D., Magnaudet, J., Ohl, C., Prosperetti, A., Tögel, R., Versluis, M. & Lohse, D. 2001 Spiraling bubbles: How acoustic and hydrodynamic forces compete. *Phys. Rev. Lett.* **86**, 4819–4822.

Saffman, P. G. 1965 The lift on a small sphere in a slow shear flow. *J. Fluid Mech.* **22**, 385. Corrigendum: **31**, p. 624, 1968.

Seddon, J. R. T. & Mullin, T. 2006 Reverse rotation of a cylinder near a wall. *Phys. Fluids* **18**, 041703.

Sridhar, G. & Katz, J. 1995 Drag and lift forces on microscopic bubbles entrained by a vortex. *Phys. Fluids* **7**, 389–399.

Taylor, G. 1928 The forces on a body placed in a curved converging stream of fluid. *Proc. R. Soc. Lond.* A **120**, 260.

Toegel, R., Luther, S. & Lohse, D. 2006 Viscosity destabilizes sonoluminescing bubbles. *Phys. Rev. Lett.* **96**, 114301.

Tomiyama, A. 2002 Transverse migration of single bubble in simple shear flows. *Chem. Engng Sci.* **57**, 1849–1858.

Tryggvason, G., Bunner, B., Esmaelli, A., Juric, D., Al-Rawahi, N., Tauber, W., Han, J., Nas, S. & Jan, Y.-J. 2001 A front-tracking method for the computations of multiphase flow. *J. Comput. Phys.* **169**, 708–759.

Yang, S. M. & Leal, L. G. 1991 A note on the memory-integral contributions to the force on an accelerating spherical drop at low Reynolds number. *Phys. Fluids* A **3**, 1822–1824.